Investigation of Coating Cracking and Fatigue Strength of 7050-T74 Aluminum Alloy with Different Anodize Coating Thicknesses

Honors Thesis

The Ohio State University
Department of Mechanical Engineering

John M. Goetz

The Ohio State University
Columbus, OH, USA
College of Engineering
Department of Mechanical Engineering

Investigation of Coating Cracking and Fatigue Strength of 7050-T74 Aluminum Alloy with Different Anodize Coating Thicknesses

Honors Thesis

John M. Goetz
7588 Lake Water Dr.
Cincinnati, OH 45242

Advisor: Dr. Mark Walter, Associate Professor
Department of Mechanical Engineering

May 20, 2005

Acknowledgements

I would like to thank my advisor, Professor Mark Walter, for his ongoing guidance on this project. Gary Gardner and Keith Rodgers in the ME machine shop have also been very helpful in machining fixtures and modifying specimens. Additionally, I would like to express my gratitude to Leslie Steele, Sam Silvers, and all those at Goodrich who have made this project possible.

Abstract

The benefits of applying anodize coatings to aluminum alloys for corrosion protection have been widely recognized. Despite their many advantages, anodize coatings are believed to be a detriment to the fatigue properties of the substrate aluminum. Additionally, there is relatively little scientific knowledge of how to optimize such coatings, and the impact of varying coating thickness is not understood.

This project involves the study of four anodize thicknesses ranges deposited on a 7050-T74 aluminum substrates. Through the use of rotary bend fatigue experiments and tensile cracking experiments, the effect of increasing anodize thickness has been examined. Scanning electron microscopy has also been used to relate the measured strengths to the cracking patterns observed at the failure surfaces. Through the fatigue experiments, it was found that the thinnest anodize coatings yielded the highest fatigue lives. The tensile cracking experiments with acoustic emission measurements indicate that when compared to the thinner coatings, the thickest coatings have a higher cohesive strength.

This research project has provided much needed insight into the field of anodic coatings for structural applications. More importantly, the results of this project quantify the extent to which the mechanical and coating properties of anodized 7050 aluminum alloy are affected by varying coating thickness. The information gained through this research project is aimed at helping Goodrich make an educated decision on the optimum thickness for the anodize coating of the 7050 aluminum alloy.

Table of Contents

List of Figures

1.Introduction/Motivation

Aluminum alloys are widely used by the aerospace industry because of their superior strength to weight ratios. However, a significant limitation for aluminum alloys is their susceptibility to corrosion. To address this problem, aluminum alloys are often treated using a process called anodizing. In this process, stable coatings are deposited on the surface of the aluminum through an electrolytic treatment. The resulting coating consists of hollow hexagonal columns of alumina (Al_2O_3). It is common to fill the pores with a sealant material. An idealized schematic of the alumina structure is given in Figure 1.

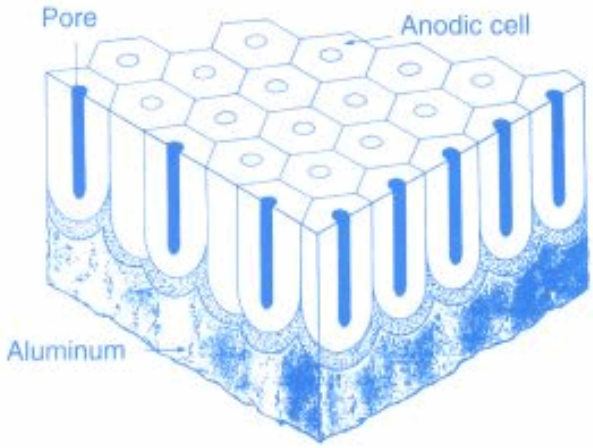

Figure 1: An idealization of the microstructure of an alumina coating formed by anodizing. [1]

The benefits of applying sulfuric anodize coatings to aluminum alloys for corrosion protection are widely recognized. Despite their many advantages, anodize coatings are also believed to reduce the fatigue properties of the substrate material. Additionally, there is relatively little scientific knowledge of how to optimize such coatings. Goodrich Corporation, a global supplier of systems and services to the aerospace and defense industry, applies anodize coatings to many components of their aircraft wheel assemblies for corrosion protection. A schematic of a typical Goodrich wheel assembly on an aircraft is given in Figure 2.

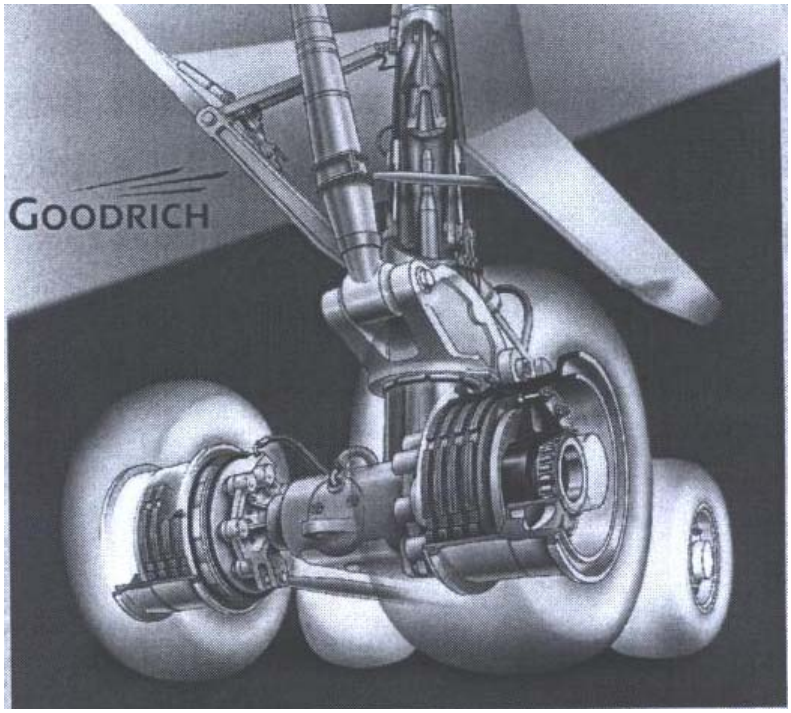

Figure 2: A typical Goodrich aircraft wheel assembly [2]

From Figure 2, it is evident that each Goodrich wheel assembly is composed of two wheel halves, a brake side and an outboard side. Figure 3 further illustrates this point with a digital photo of a Goodrich wheel cutout. The two halves of the wheel assembly have different stress and heat requirements and are therefore made from different alloys. The brake side is composed of anodized 2014-T6 aluminum to account for the increased heat from braking friction, while the outboard side is made from anodize coated 7050-T74 aluminum alloy. Goodrich's thickness specifications for the anodize coating have varied greatly over the last ten years and it is unclear how anodize thickness affects the fatigue properties of 7050-T74 aluminum. To address these concerns, Goodrich Corporation has sponsored this project to examine the effects of anodize coating thickness on mechanical properties.

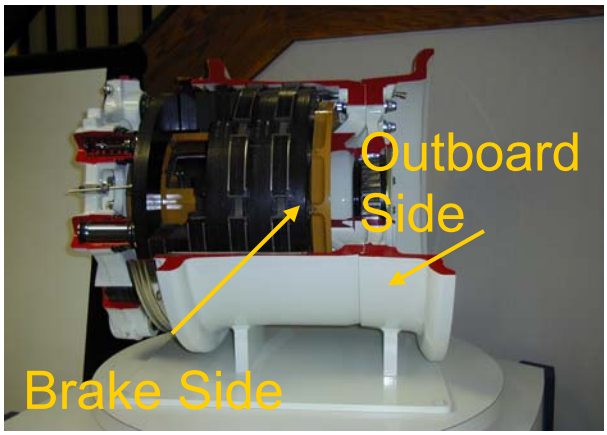

Figure 3: A photo illustrating two halves of a Goodrich wheel

2. Background

2.1 Fatigue Theory

The vast majority of practical engineering design applications involve fluctuating or cyclic loads well below the yield stress of the material of interest. Despite the low magnitude of these stresses, damage can accumulate and "fatigue failure" can occur. It is estimated that over 80 percent of all brittle fractures involve some period of fatigue crack growth [3]. The rotation of a loaded aircraft wheel during landing is just one area of application in which the study of fatigue failure is relevant.

Depending on the stress amplitude applied to the material, two distinct classes of fatigue are recognized. Low-cycle fatigue is characterized by high stress levels and total life spans on the order of 1000 cycles. In contrast, high cycle fatigue occurs with loads far below the yield stress and results in a longer lifetime before failure. Because high-cycle fatigue is more typical in applications, it is usually more germane to engineers. High cycle fatigue consists of three distinct stages: crack initiation, crack propagation, and a period of unstable, rapid crack growth leading to failure [4]. The three stages of fatigue cracking are illustrated in Figure 4, a log plot of da/dN (change in crack length over change in cycles) versus the change in the stress intensity factor, ΔK.

In most cases fatigue cracks initiate at the surface of a material where microscale stress raisers are likely to exist. Macroscale surface defects such as scratches, sharp fillets, keyways, threads, dents, or other similar phenomenon are common and represent

additional stress concentrations at the surface. Although surface nucleation sites are the most common, it is possible for cracks to form subsurface if inclusions or voids are present in the interior of the material. Regardless of the location of nucleation, it is important to note that fatigue cracking always initiates from a material or structural defect. If no stress raisers exist initially, the "back and forth" motion caused by cyclic

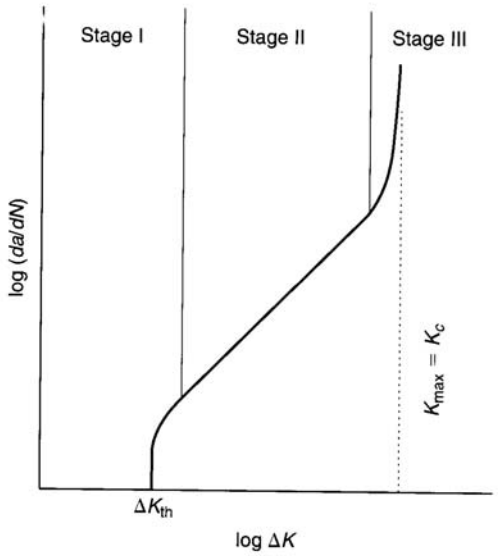

Figure 4: Fatigue crack growth curve over full range of applied ΔK [3]

loading can produce microscopic surface discontinuities. This mechanism, known as fine slip, occurs when submicron displacements are formed by the activation of dislocation motion in grains [3]. The resulting peaks and notches seen in Figure 5 are called dislocation slip steps. Because of their shapes, such steps may also act as stress raisers, causing cracks to initiate at the surface.

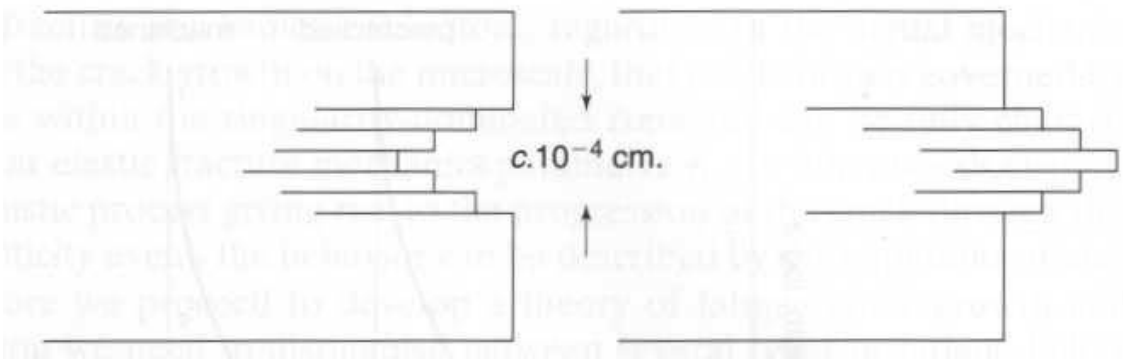

Figure 5: Notch and peak slip steps formed from fine slip [3]

After the initial micro-cracks initiate, they continue to propagate through the material as cycling continues. This phenomenon is often referred to as stage II cracking. The stage II crack propagation stage is characterized by two types of markings, termed beachmarks and striations. Beachmarks are visible on the fracture surface with the naked eye and represent a single period of time over which crack growth occurs. Fatigue striations are microscopic in size and represent the progression of the crack front during one load cycle [5]. When present, either of these markings are a good indication that part failed in fatigue loading. Also, because they extend outward from and point back to the initiation site, the markings are very useful in locating the exact point of nucleation. Figure 6 demonstrates how striations can be used to locate the nucleation point. Once the initiation site is located, it can be closely analyzed using scanning electron microscopy (SEM) to determine the cause of crack initiation.

Stage III of fatigue failure occurs when the fatigue crack reaches a critical length. In this stage, the cracks approach the critical crack length and advance rapidly during one monotonic loading cycle. Despite having loaded the body at relatively low loads, eventually rapid brittle failure occurs suddenly and often without any obvious external warning signs. The catastrophic and unpredictable nature of fatigue failure has led to a continued commitment by engineers to fully understand the process of fatigue.

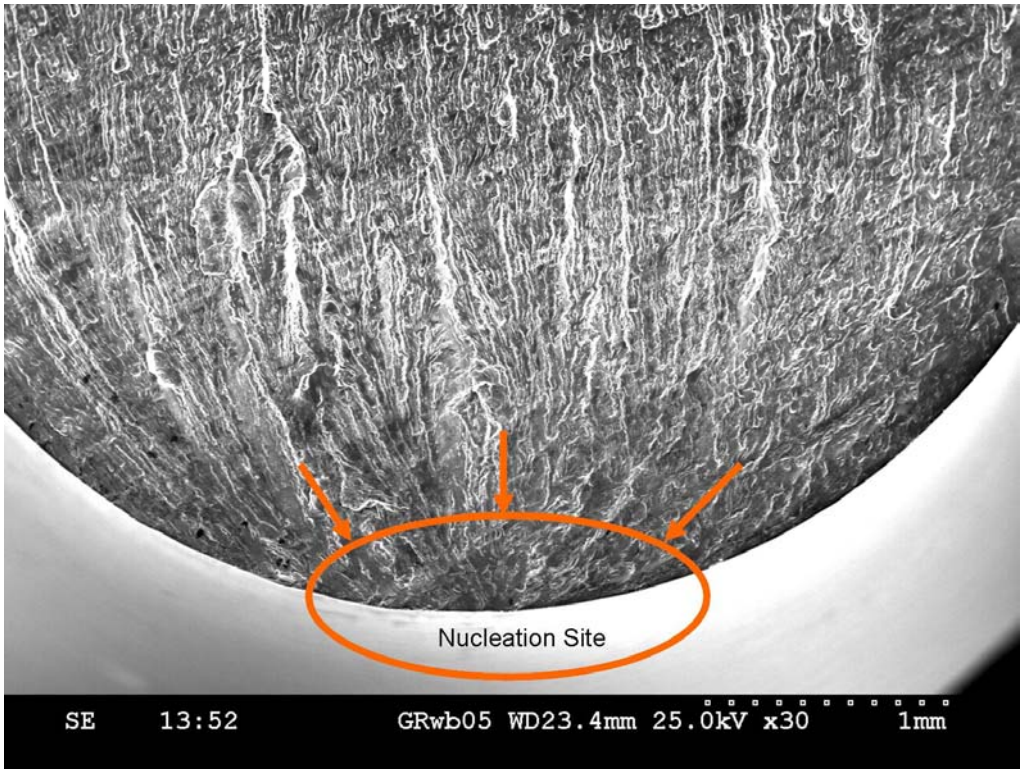

Figure 6: Beachmarks indicating the nucleation site for 7050 T-6 aluminum fatigue specimen

The most common method for analysis and subsequent prediction of fatigue failure focuses on the amplitude of the cyclic stress versus the overall life of the material. This approach is called "S-N curve" analysis. Typically the number of cycles to failure is plotted on the x-axis on a log scale, while the stress amplitude is plotted on the y-axis. Stress amplitude is defined according to equation 1.

Equation 1

$$\sigma_a = \frac{\sigma_{\max} - \sigma_{\min}}{2}$$

In this equation, σ_a is the stress amplitude, $\sigma_{\max}$ is the maximum normal stress during cycling, and $\sigma_{\min}$ is the minimum normal stress during cycling.

Due to the statistical nature of fatigue, it is necessary to use the results of many fatigue experiments at a given load to find a single representative value for the number of cycles to failure. Therefore, each point on a standard S-N curve represents a series of

fatigue experiments. If a large number of samples are run, confidence intervals can give accurate predictions of the fatigue life at a given load. If smaller numbers of samples are run, simply taking the average is a less precise, but acceptable alternative. Although S-N curves are effective at predicting the number of cycles to failure, it is worthwhile to note that fatigue behavior can be extremely sensitive to many variables in addition to the stress amplitude.

The most obvious of these other variables is the effect of mean cyclic stress on the life of the specimen. Mean cyclic stress is defined according to equation 2. In general, increasing the mean stress tends to lead to a reduction in fatigue life.

Equation 2

$$\sigma_m = \frac{\sigma_{\min} + \sigma_{\max}}{2}$$

where σ_m is the mean cyclic stress. Another variable for fatigue loading is known as the stress ratio, *R*. *R* is defined according to equation 3.

Equation 3

$$R = \frac{\sigma_{\min}}{\sigma_{\max}}$$

A common loading situation seen in many engineering applications is known as completely reversed loading. Completely reversed cycling occurs when a specimen is loaded equally in tension and compression during each cycle. For this situation, according to equation 2 and 3, σ_m =0 and R=-1. The rotation of an aircraft wheel is just one example of an application experiencing completely reversed loading. Rotating cantilever bend machines used for fatigue experimentation must operate under completely reversed loading. Axial fatigue machines are not limited to completely reversed loading, and the mean cyclic stress can be set to any desired value. Other factors affecting the fatigue life of a material are its surface finish and its susceptibility to corrosion.

As previously mentioned, the surface profile of the part undergoing fatigue loading is extremely important. Any defects on the surface of a material can act as stress raisers, thereby limiting the fatigue life of the specimen. For this reason, parts experiencing

fatigue are often polished to improve their surface characteristics. Corrosive environments can cause small pits to form on the surface of certain materials. These pits act as stress raisers and crack nucleation points. Additionally, the hydrogen present in corrosive environments tends to increase the crack propagation rate. As demonstrated in Figure 7, aluminum alloys are particularly susceptible to corrosion due to their high electrical potential value. This fact together with the widespread use of aluminum alloys drives the need for methods to protect aluminum alloys from corrosive degradation.

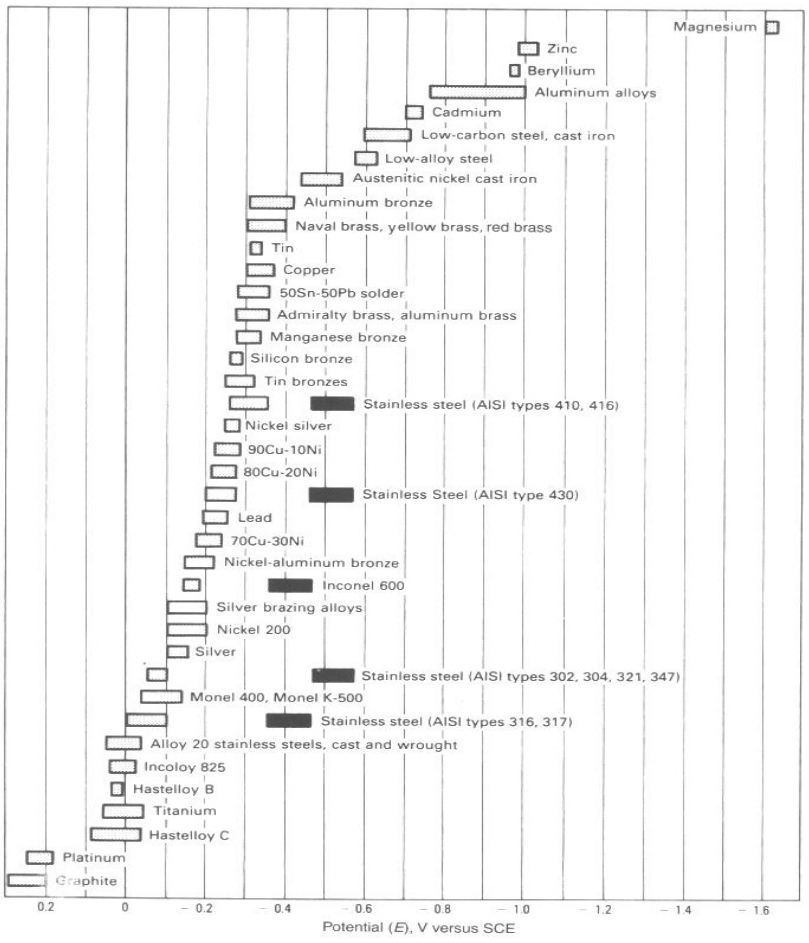

Figure 7: Standard emf series for various metals [6]

2.2 Anodizing Theory

Aluminum and its alloys naturally form a protective aluminum oxide (alumina or Al_2O_3) layer when exposed to air. However, this layer is extremely thin and not very adherent [7]. Thus, for practical applications, the naturally formed alumina coating does

not provide adequate corrosion protection. Aircraft wheels for example face a wide range of severe weather, temperatures, chemical environments, and wear conditions. In order to form a more durable coating that provides the necessary protection, aluminum aircraft wheels undergo a treatment known as anodizing.

Anodizing is defined as the electrolytic treatment of metals, where stable films are deposited on the surface of the metal. Although many types of anodizing processes exist, cast aluminum parts such as aircraft wheels usually undergo a treatment known as batch anodizing [8]. In this process, a barrier oxide layer is formed on the aluminum substrate by passing an electrical current through an acid electrolyte bath in which the aluminum is immersed. Goodrich Corporation uses a sulfuric acid solution to anodize all of the structural components of their aircraft wheels. The name anodizing exists because the metal being coated acts as the anode in a voltaic cell. A general schematic of a voltaic cell is given in Figure 8.

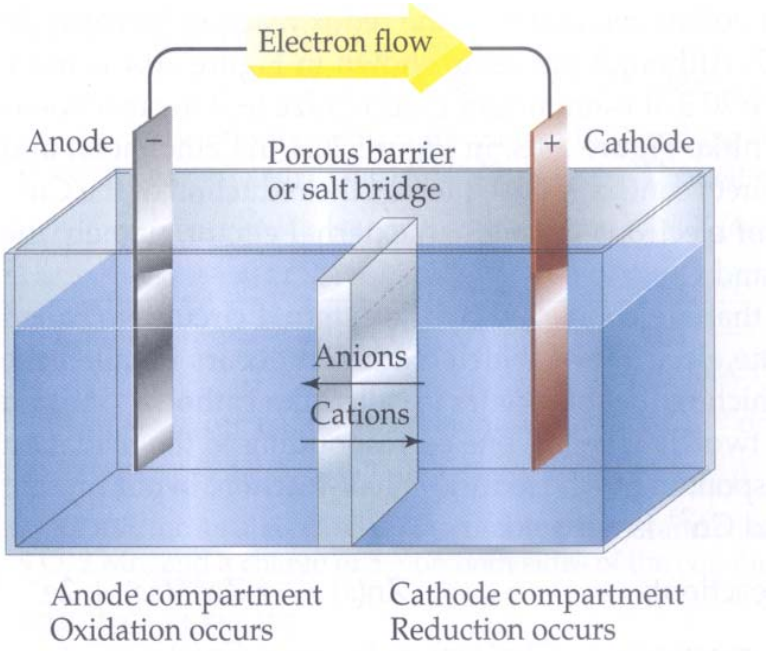

Figure 8: Schematic of a general voltaic cell [6]

The thickness of the deposited anodize coating can be varied by controlling the applied current density (amps/in^2) and by the time of anodizing. Upon closing the circuit, electrons flow from the anode to the cathode leaving aluminum cations at the surface of

the alloy. These cations react with water in the electrolytic solution to form an alumina layer on the surface of the alloy. The overall reaction is summarized in Figure 9.

The resulting alumina structure is a hexagonal cellular matrix. Each cell in this matrix is anywhere from 50 to 300 nanometers wide, is columnar, and contains with a single central pore on the order of 25 to 150 nanometers in diameter [8]. A very thin non-porous barrier layer also exists at the base of the columnar structure. An idealized schematic of the alumina microstructure was provided in Figure 1. It should be noted that the actual microstructure of the alumina coating will be affected by a variety of parameters used in the coating process. A sealant is often used to fill in the naturally occurring pores and to further enhance the corrosion resistance of the coating. The standard sealant used by Goodrich is a dichromate seal.

$$2Al \rightarrow 2Al^{3+} + 6e^-$$
$$2Al^{3+} + 3H_2O \rightarrow Al_2O_3 + 6H^+$$
$$6H^+ + 6e^- \rightarrow 3H_2$$

$$2Al + 3H_2O \rightarrow Al_2O_3 + 3H_2$$

Figure 9: Anodizing reaction to form alumina coating

2.3 Tensile Cracking

For any coating system, the adhesion strength of the coating-substrate interface is a key determinant of the overall lifetime of the part. Cracking of such coatings begins when the tensile stress on the system exceeds a critical value [9]. In the vicinity of the crack, stresses on the coating are relieved. However, shear stresses are transmitted across the interface and as one moves away from the crack, the normal stress in the coating begins to build up. As shown in Figure 10, this eventually leads to the development of an array of transverse that are perpendicular to the loading direction.

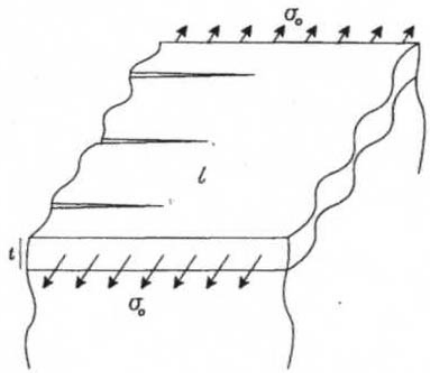

Figure 10: Formation of transverse cracks in brittle coating under uniaxial tension [9]

Four distinct stages of transverse crack growth have been identified in the literature and can be seen graphically in Figure 11. They include multiplication, stabilization, cross-linking, and spallation [10]. At the end of the stabilization stage on the graph, the curve begins to flatten out, representing the point at which the coating is saturated with cracks. A method described in the literature to evaluate the adhesion strength of thin films calls for a measurement of the inter-crack spacing when crack saturation occurs [11].

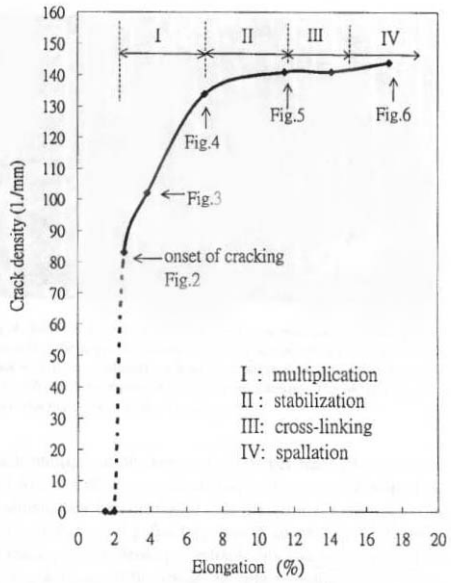

Figure 11: Four stages of crack propagation in brittle films [10]

The shear-lag theory can be implemented to determine the maximum shear stress across the interface [12,13] This requires measuring the tensile strength of the coating and the crack spacing. These experimentally determined values are related to the interfacial shear stress of the coating-substrate interface using equation 4,

Equation 4

$$\hat{\tau} = \frac{\pi \delta \hat{\sigma}}{\hat{\lambda}}$$

where, $\hat{\tau}$ is the ultimate interfacial shear strength of coating, δ is the coating thickness, $\hat{\sigma}$ is the tensile strength of the coating, and $\hat{\lambda}$ is the maximum inter-crack spacing present during crack saturation. It should be noted when using this equation, that $\hat{\sigma} = E_c \varepsilon_f$, where E is the Young's Modulus of the coating and ε_f is the strain at which cracking begins. Although others have used in situ microscopy to determine ε_f, it is expected that acoustic emission analysis could be employed to determine the point at which cracking begins.

2.4 Acoustic Emission (AE)

Acoustic emission is a widely recognized technique used to monitor and predict material failure in structures. It operates by sensing low-level seismic signals caused by sudden release of mechanical energy in the material of interest [14]. Nearly all causes of AE are damage related. Therefore, the measurement of acoustic emission counts, events, and energies can be related to defect formation and failure. AE is normally measured by placing a small piezoelectric-based transducer on the specimen of interest. Despite the name, AE generally does not occur at a frequency that can be detected by the human ear. Most AE events produce waves which range from 100-400 kHz. Since the output of the piezoelectric element inside the transducer is so small, the signal must be amplified and filtered before being collected by a special data acquisition system. A schematic of a typical AE setup is shown in Figure 12.

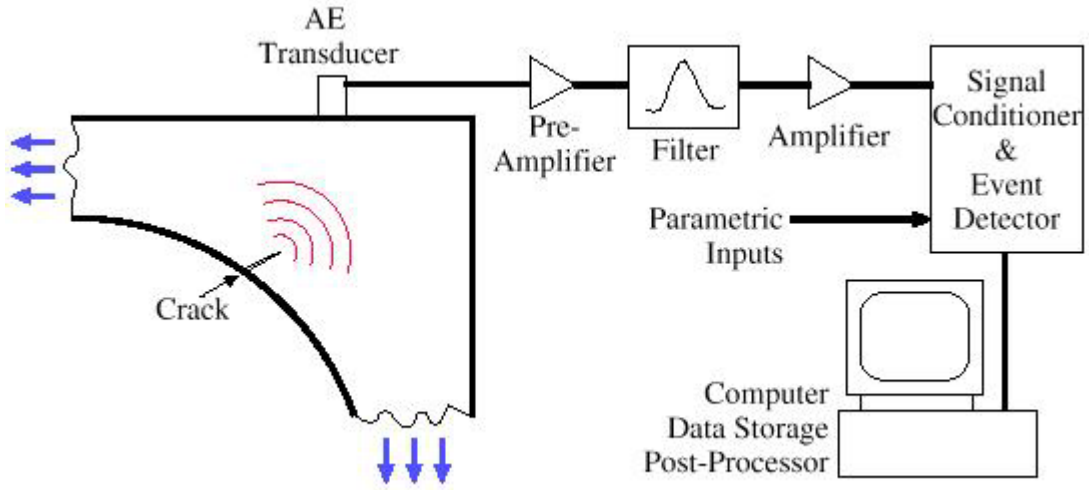

Figure 12: Standard hardware setup for acoustic emissions experimentation [14]

AE events or "hits" are recorded when the transducer detects a signal with a magnitude above a preset threshold energy value. A single AE event is composed of any number of counts or threshold crossings. A schematic illustrating several AE parameters associated with an event is given in Figure 13.

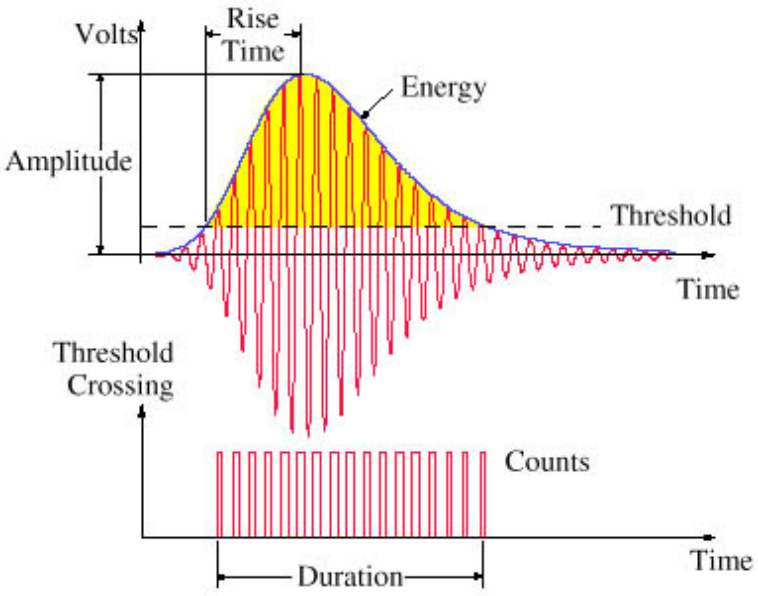

Figure 13: Schematic Defining Common AE terms [14]

For this project, it has been attempted to use cumulative acoustic emission counts and the first high-count AE event to detect the strain at which transverse cracks begin to form in the anodize coating (ε_f). Although AE is an extremely valuable experimental method, it is not without some drawbacks. For example, because data is recorded for any signal above the threshold value, AE systems are very susceptible to noise. Noise is defined as any process or phenomenon that can mask or be mistaken for the desired signal [15]. Precautions against noise must be taken whenever working with AE. Some strategies that may be taken to limit noise in a system are isolating the test area, using shielded cables, securing all loose parts, and separating surfaces in free contact. For tensile testing, the type of grip can also determine the amount of noise in the system. Wedge grips, for example are very noisy and tend to produce AE throughout the duration of an experiment. More favorably, constant force grips, such as pin grips tend to concentrate noise at the moment of gripping only. This normally occurs early in the test. The type of tensile testing machine can also have an impact on the level of noise in the system. For example, hydraulic driven testing machines produce far more noise than screw driven machines.

3. Experimental Setup

3.1 Fatigue Testing

To experimentally investigate fatigue properties of 7050-T74 aluminum alloy, specimens were subjected to cyclic loading conditions to induce failure. Ideally the loading conditions induced by the experimental apparatus should simulate those seen in actual aircraft wheel applications, such as landing or taxiing. With proper specimen design, the Krouse 200 in-lb rotating cantilever beam machine at Ohio State is capable of producing the alternating tensile and compressive stresses developed in these applications. With the rotary cantilever machine, the specimens undergo a constant rotational speed where the maximum stresses are found on the surface. A digital photo and a detailed schematic of the Krouse machine can be seen in Figures 14 and 15.

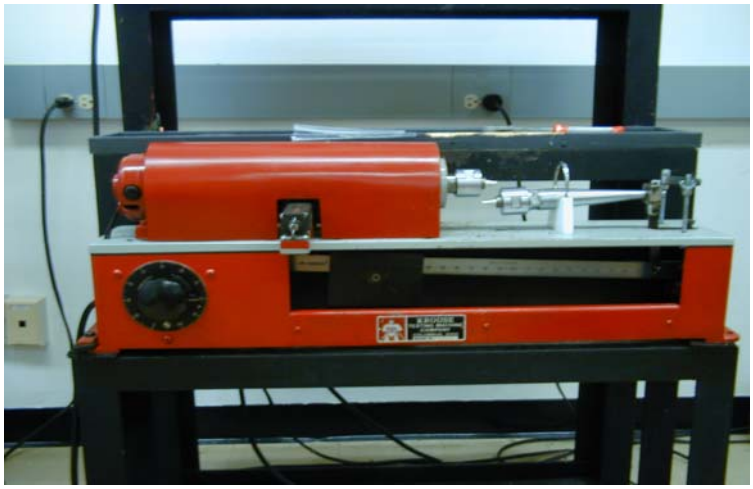

Figure 14: Photo showing Krouse 200 in-lb rotating cantilever beam machine

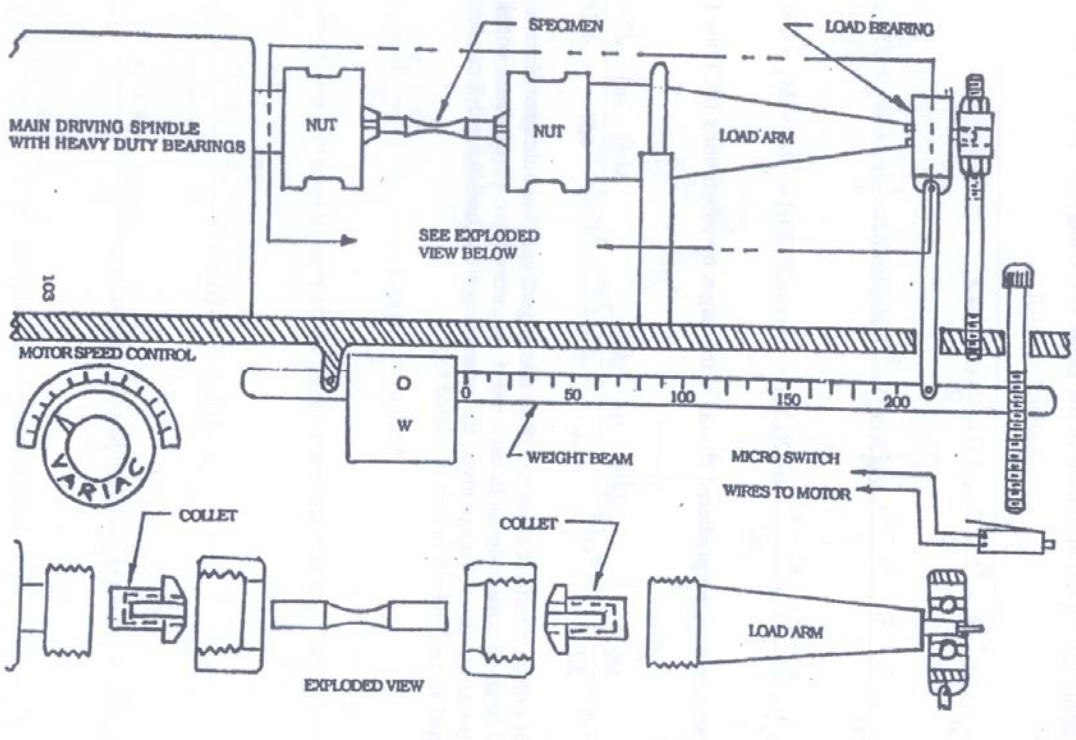

Figure 15: A detailed schematic showing the operation of the Krouse fatigue machine [16]

Cylindrical fatigue specimens are clamped into the Krouse using a set of two freely

rotating collets. One of these collets is connected to a small DC motor, while the other is connected to a load arm. Using a sliding weight, a moment can be applied to the specimen at the end of the load arm. The moment is related to the applied stress through standard strength of materials. In equation 5 the bending stress equation is manipulated to include the moment of inertia in terms of the diameter of the specimen *D*. In this way, given the specimen diameter and the desired stress, σ, the required moment can be calculated.

Equation 5

$$M = \frac{\sigma \pi D^3}{32} = .0982 \sigma D^3$$

To insure that the desired stress level was accurately obtained, each of the experimental setups needed to be calibrated. As shown in Figure 16, a strain gage was installed on a dummy 7075 Al alloy test specimen to determine the appropriate position in the collets. The dimensions of the dummy specimen used were identical to the

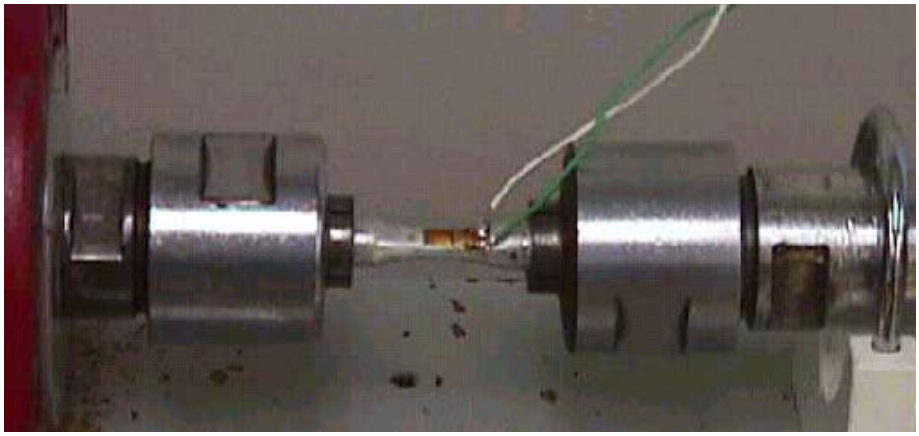

Figure 16: Strain gage/dummy specimen setup used to calibrate Krouse machines

7050 T-74 specimens. To find the maximum tensile strain, the specimen was loaded with an arbitrary moment and manually rotated until a maximum value was read on a P3500 Measurements Group Incorporated strain indicator. A digital photo of the strain indicator is given in Figure 17.

Figure 17: P3500 strain indicator used to calibrate Krouse machines

Once the maximum strain was found, the load was removed and the strain gage was zeroed using the knob on the indicator. Finally, without moving the specimen, a known bending stress was applied and strain was recorded. Stresses from the strain gage were calculated using Hooke's Law and an elastic modulus of 10.3×10^6 psi. These values were then compared to the stress value that was set with the applied moment. After a number of measurements were taken, it was found that specimens could be loaded very closely to the theoretical value for all three experimental setups.

A drawing of the specimens used in the Krouse experiments is given in Figure 18. Goodrich worked with Hohman Plating to anodize the specimens to four different thickness ranges, (0.0-0.2 mil, 0.3-0.5 mil, 0.5-0.7 mil, and 0.7-0.9 mil). The material for the specimens was excised from the flange and mating sides of the outboard side of the wheel assembly. Twenty specimens were anodized for each thickness range. One of these twenty was used to check that the coating thickness was within the desired range.

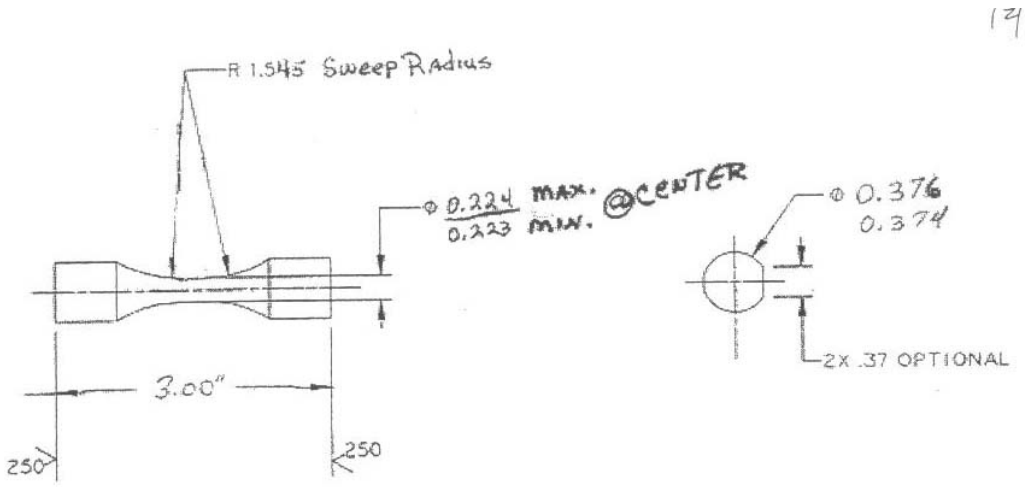

Figure 18: Engineering drawing of the cylindrical fatigue specimens

Once the specimens were machined and the calibration of the setup was complete, experimentation began. Each coating thickness was loaded in the range of 30 ksi to 50 ksi. The loaded end of the specimen was held in place by a bearing assembly while the weight on the slider arm was set. Once the load was set, the motor was turned on using a variable speed control. In order to meet time constraints on the project, the speed of the motor was held constant for all experiments at 80% power. This correlated to a rotational speed of approximately 232 Hz. Once the motor was up to speed, the support bearing was disengaged and the specimen was loaded. As the motor rotated at a constant rate, the specimens experienced completely reversed cyclic loading until failure. At the point of failure, the machine was automatically switched off. The number of cycles to failure was recorded from a counter, which was directly geared to the motor. Because the counter was geared to the motor, the approximate number of rotations occurring after the failure of the specimen but before the motor came to a complete stop were subtracted from the total. The average number of cycles subtracted for spin down was between 1400 and 1500 depending on the machine used. The number of samples to run for each data set was determined by the observed fatigue life of the first sample in the set. If there were relatively few cycles to failure (life less than 10000 cycles) then three total experiments were conducted. If there were a large number of cycles to failure, then five experiments

were conducted. This was done to conserve the number specimens by not repeating low cycle experiments, which are characterized by less scatter.

After the specimens had been run, a scanning electron microscope (SEM) was used to observe cracking patterns on the fatigue failure surface. The Hitachi Instruments S-3500N SEM at Goodrich Wheel and Brakes in Troy, OH was used for these observations. A digital photo of the SEM is given in Figure 19.

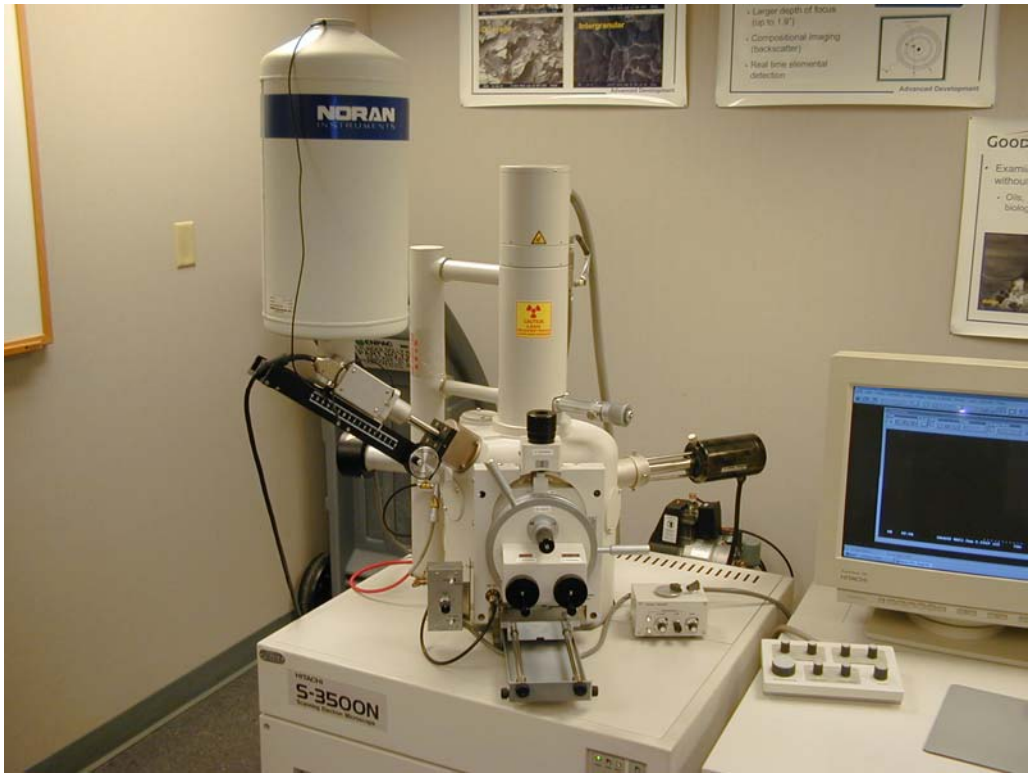

Figure 19: Scanning electron microscope at Goodrich.

To prepare the specimens for viewing, a Leco slow-speed, diamond tip saw was used to cut the specimens to an appropriate size. Carbon paint was then used to electrically link the specimens to small aluminum viewing discs. A group of specimens ready for viewing can be seen in Figure 20.

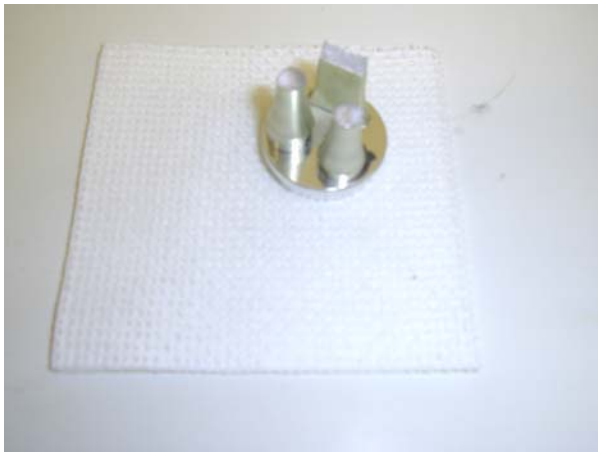

Figure 20: SEM specimens on aluminum viewing disc

3.2 Tensile Cracking

To obtain a measurement of the cohesive strength of the coating, tensile cracking experiments were conducted. In these experiments, a dog-boned tensile specimen was gripped at either end and pulled in uniaxial tension. The specimens designed for this set of experiments is shown in Figure 21.

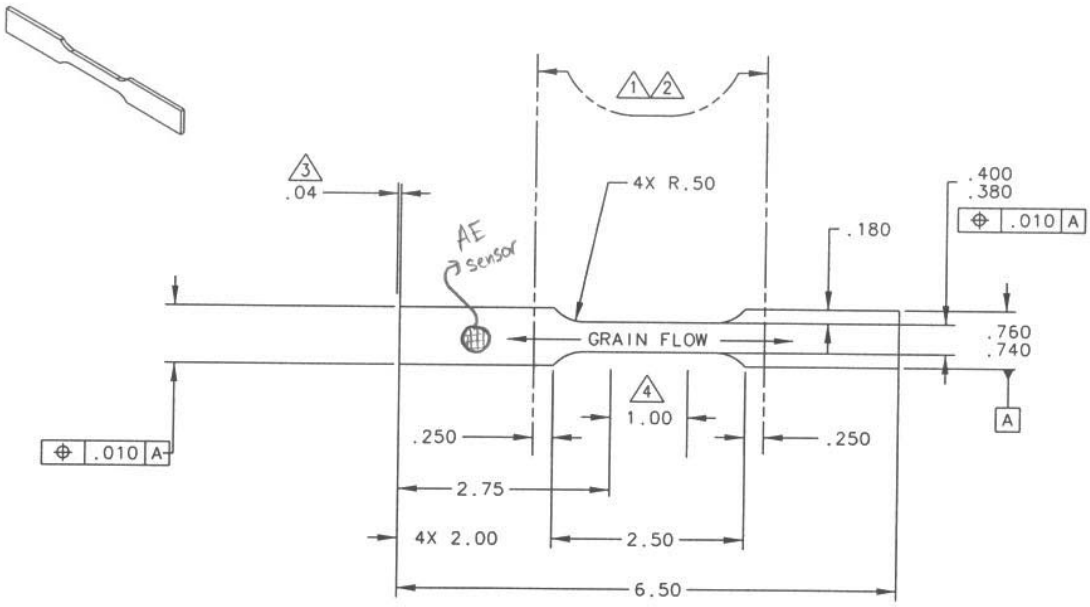

Figure 21: Tensile specimens used for tensile cracking experiments

The tensile specimens were also anodized by Hohman Plating to the same four thickness ranges used in the fatigue tests. The experiments were first attempted on an MTS hydraulic machine at OSU. It was determined, however, that the hydraulic load frame introduced too much extraneous noise into the AE measurements. Therefore, an Instron screw machine, which was known to be much quieter, was used for the remainder of the tensile cracking experiments. The specimens were originally designed to be used with wedge grips. However, it was decided that the wedge grips were creating additional acoustic noise due to relative motion of parts in the grip. A set of dual-pin grips was designed and the specimens were modified to fit these new grips.

Prior to running an experiment, each specimen was instrumented to measure stress, strain, and acoustic emission data. A 5000 lb load cell built into the upper cross-head of the Instron measured the applied force. Applied force could then be converted to tensile stress using the specimen's cross sectional area. Stain measurements were collected using an MTS clip extensometer connected to a P3500 strain indicator. The extensometer was attached to the specimen using rubber bands. The extensometer's locking pin was used to fix the initial length of the extensometer to one inch. Since strain is change in length divided by original length and the original length is 1 inch, the strain calculation simply required knowing the change in length in inches. To convert the voltage output of the extensometer to a displacement measurement, the extensometer was calibrated using the setup shown in Figure 22.

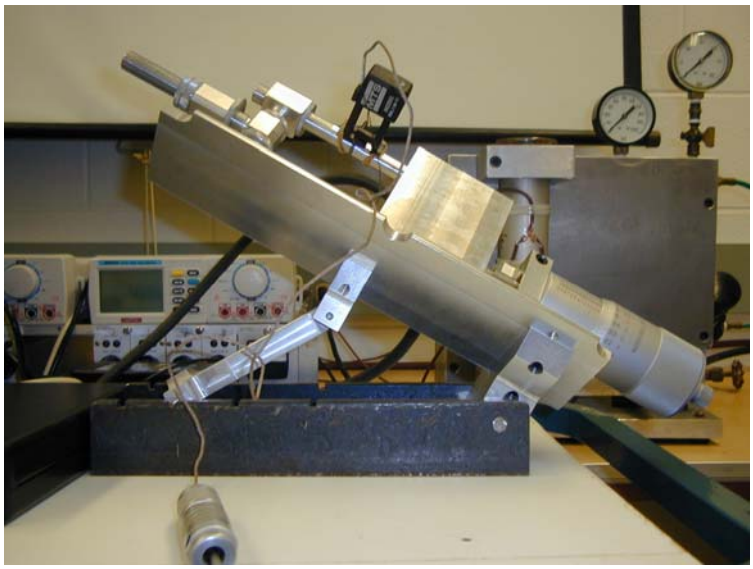

Figure 22: Device used to calibrate MTS extensometer

To set up the calibration, the extensometer was clipped to a fixed rod and to a rod that was attached to a moving block. The movement of the block was controlled by gravity and a rotating barrel micrometer. One rotation of the micrometer corresponded to a displacement of 0.0025 inches. The change in output voltage was then recorded for a series of micrometer rotations. After taking fourteen increasing and decreasing voltage readings for the .0025 inch displacement steps, an average calibration factor was determined (change in length/change in voltage). A calibration plot used to obtain this factor is given in Figure 23.

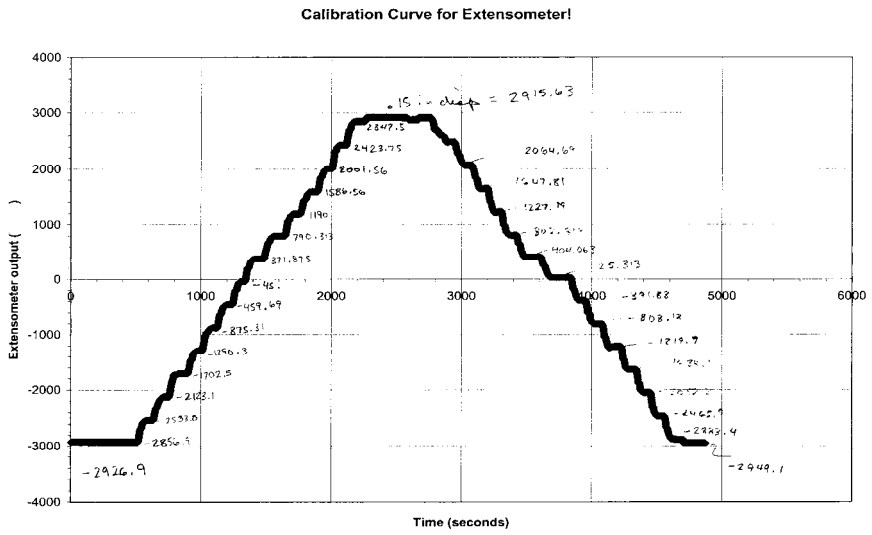

Figure 23: Calibration curve for clip extensometer

Acoustic emission counts were measured using a small piezo-electric sensor on the surface of the specimen. Although a variety of methods to attach the AE sensor to the specimen were examined, vacuum grease and a set of rubber bands offered the most effective yet simple solution. The output signals of the load cell, extensometer, and AE sensor were acquired using the Vallen AMSY-5 AE system. This system is capable of recording AE data concurrently with up to 4 external voltage signals. As will be described in the next section, the acquired data was used to investigate the strain at the onset of crack formation in the coating. A digital photo of the complete tensile cracking setup is given in Figure 24.

Preparation for SEM for the tensile cracking specimens was nearly identical to the procedure followed for the fatigue specimens. The only difference was that tensile cracking specimens were oriented so that the cracks in the anodize coating could be imaged.

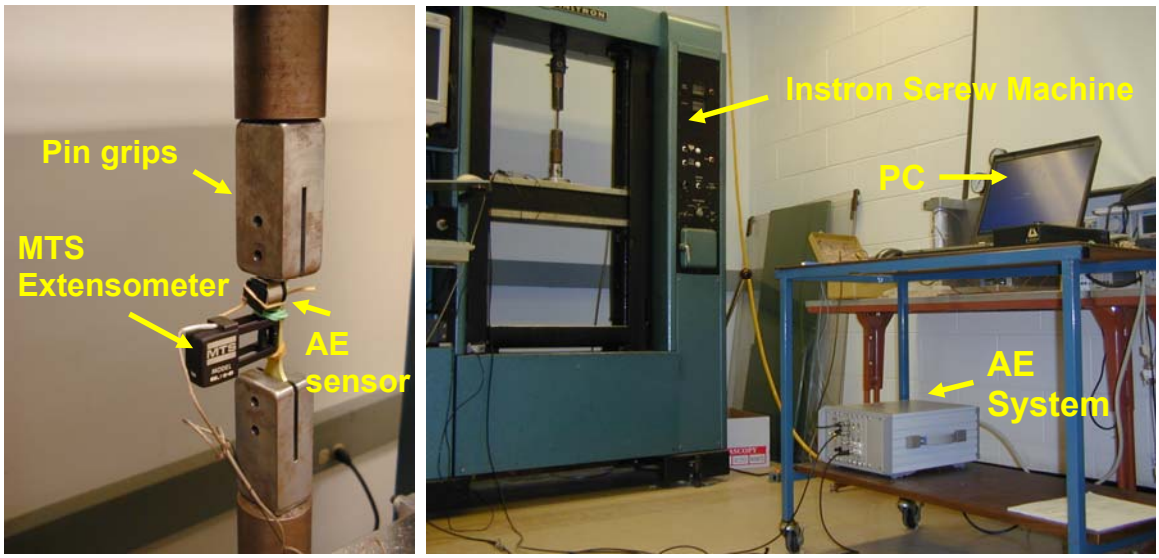

(a) Grips, specimen and sensors (b) Instron and data acquisition system

Figure 24: Tensile cracking experimental setup

Prior to running the experiment, a list of various parameters was checked. A constant displacement rate of 0.01 inches per minute was set by adjusting the gearing of the Instron screw machine. A preload of approximately 20 pounds was also applied to each specimen. This prevented any slip of the extensometer and reduced the number of AE events attributed to gripping. Immediately prior to testing, the AE threshold was also set. A constant threshold of 37.3 dB was deemed appropriate for all coating thicknesses except 0.0-0.2 mil. The 0.0-0.2 mil specimens were quieter in general and required a lower threshold of 31.3 dB. Finally, the pin in the extensometer was removed and the test was begun. During the test, the AE data and parametric data were monitored using Vallen's Visual AE software. The test was halted when it appeared that the cumulative AE counts had reached a saturation point.

4. Experimental Results and Discussion

4.1 Fatigue Testing Results

7050-T74 aluminum fatigue specimens for each of the four anodize thickness ranges (0.0-0.2, 0.3-0.5, 0.5-0.7, and 0.7-0.9 mils) were cyclically loaded using the Krouse 200 in-lb rotating cantilever beam machine. A more detailed description of the experimental setup and methodology were discussed in Section 3.1. The results from the rotating cantilever beam fatigue experiments for the four anodize thickness ranges are shown on the S-N diagram in Figure 25.

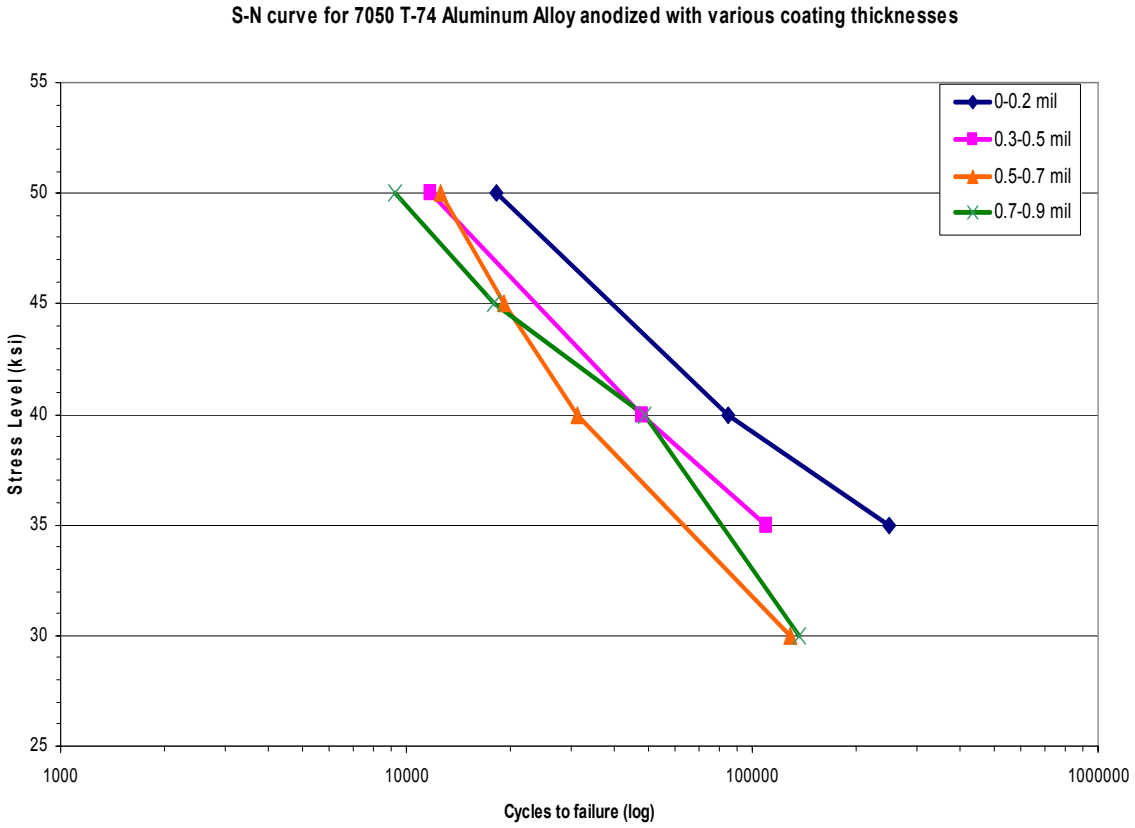

Figure 25: S-N curves for the four anodize coating thickness ranges studied

In Figure 12, the alternating stress amplitude is plotted on the y-axis in units of ksi and cycles to failure are plotted on a log x-scale. Recall that each point on this diagram

represents the average of a series of three to five fatigue experiments at a given alternating stress amplitude. Prior to plotting and averaging, outlying fatigue life values were identified and eliminated from the data set. An outlier was classified as a specimen with a fatigue life above or below three standard deviations from the mean.

From the S-N curve, it is evident that there is a relationship between the fatigue life and the thickness of the anodize coating. First of all, when comparing the 0.0-0.2 mil coating thickness, to the 0.3-0.5 mil coating thickness, it is clear that 0.0-0.2 mil specimens have a significantly longer fatigue life. Although not as significant, this trend extends to the 0.5-0.7 mil coating thickness as well, which has an even further reduced fatigue life. The 0.7-0.9 mil specimens do not follow the trend of reducing fatigue life. Thus, the data suggests that increasing coating thickness beyond 0.7 mil does not have a further degrading effect on the fatigue life of the specimen.

After completing the fatigue experiments, scanning electron microscopy (SEM) was used to examine the failure surfaces of the fatigue specimens. The failure surfaces were inspected to see if any microstructural features could be correlated to the results shown in the S-N curve and the reduction in fatigue life with increasing coating thickness. Approximately four specimens per coating thickness were observed, as well as all outlier specimens. Although no significant differences could be correlated to coating thickness, distinct types of cracking patterns were related to the stress amplitude at which the specimens were run. The failure surfaces of specimens run at loads below 30 ksi, were characterized by single crack initiation points at the surface of the specimen. These initiation points are located by following beachmarks on the specimen. Those specimens run above 45 ksi exhibited multiple nucleation points at the surface. Figure 26 illustrates the two observed types of failure surfaces.

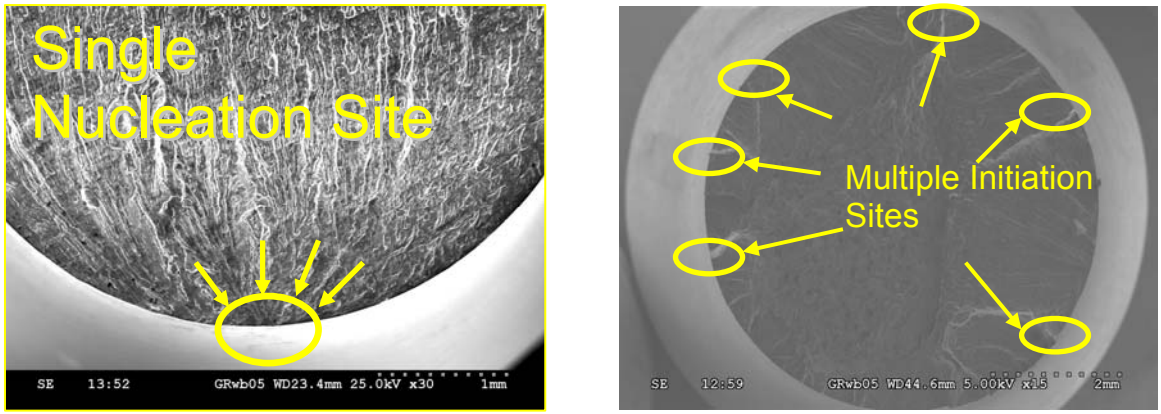

(a) (b)

Figure 26: Observed failure surfaces for (a) low and (b) high stress amplitudes

This behavior can be explained by the existence of different initial defect sizes. At low loads only the largest defects are "activated." At high loads a larger range of defects are activated and therefore there are higher chances of multiple initiation sites. In addition, since the Krouse 200 in-lb rotating cantilever beam machine subjects the entire circumference of the specimen to the maximum and minimum bending stress, further opportunities exist for critical defects to form at the surface. Failure initiation at the surface also can be linked to defects in the anodize coating. All observed specimens with surface nucleation sites exhibited some type of crack or defect in the anodize coating. Figure 27 illustrates some typical types of microscopic defects seen in the anodize coating.

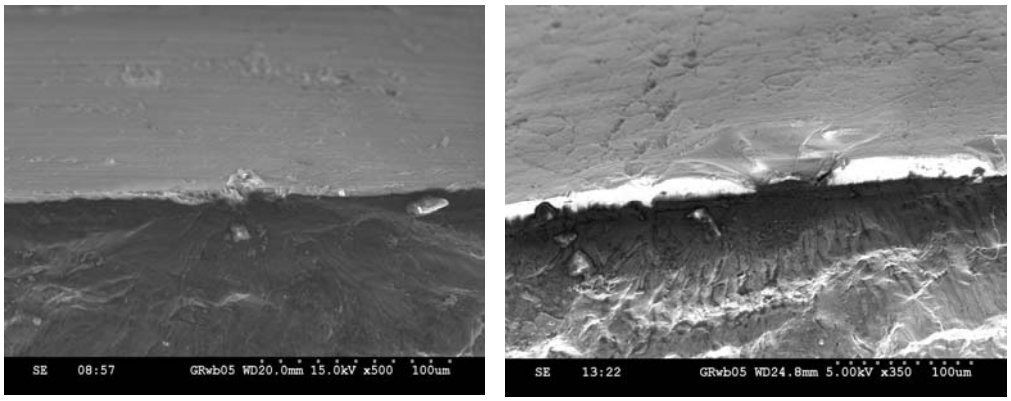

(a) 0.0-0.2 mil coating run at 30 ksi (b) 0.7-0.9 mil coating run at 30 ksi

Figure 27: Defects at nucleation sites in two different anodize coatings

4.2 Tensile Cracking Results

Tensile cracking experiments were conducted using the 7050-T74 aluminum tensile specimens described in Section 3.2. For each range of coating thickness, two to three experiments were conducted. Although some experiments were run to higher strain levels, all curves presented below are truncated at ε=0.045. Cumulative acoustic emission counts were obtained from the Vallen AE software and were normalized in the manner described below. The voltage output of the extensometer was converted to strain via the calibration process described in Section 3.2. Stress in units of MPa was calculated using load cell readings and the specimen's cross-sectional area. The results from all of the specimens for each of the four thickness levels can be seen in Figures 28-31.

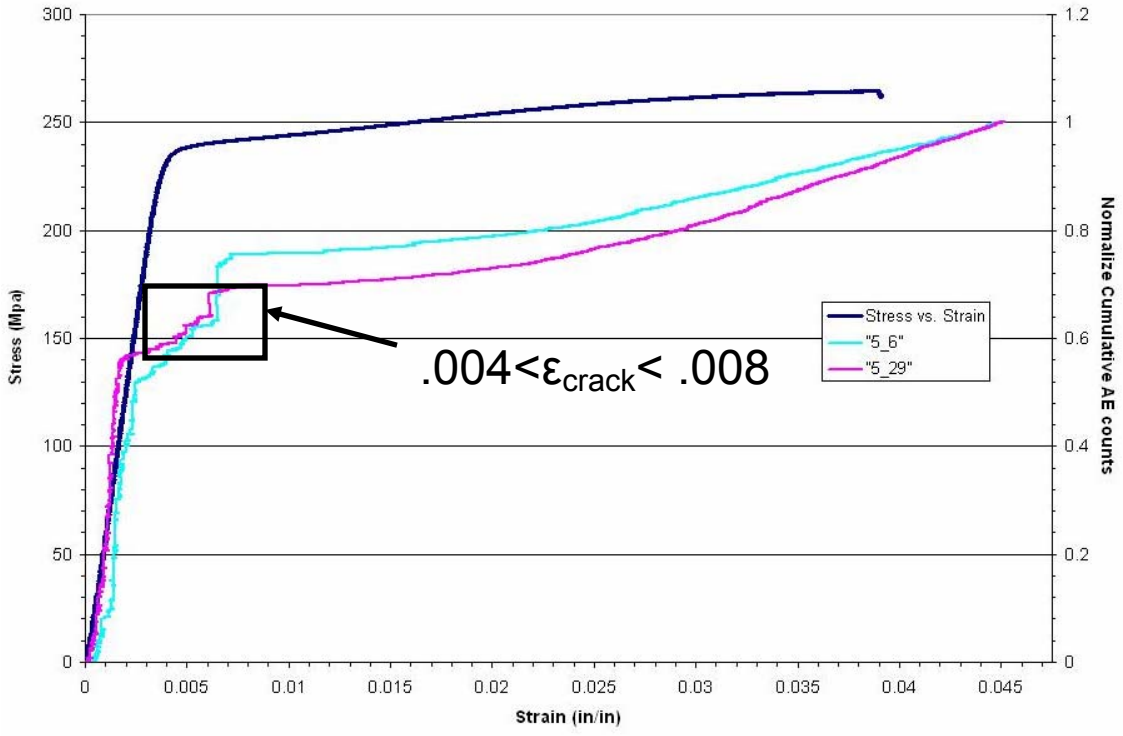

Figure 28: Cumulative normalized AE counts versus strain for all specimens with a coating thickness of 0.0-0.2 mil

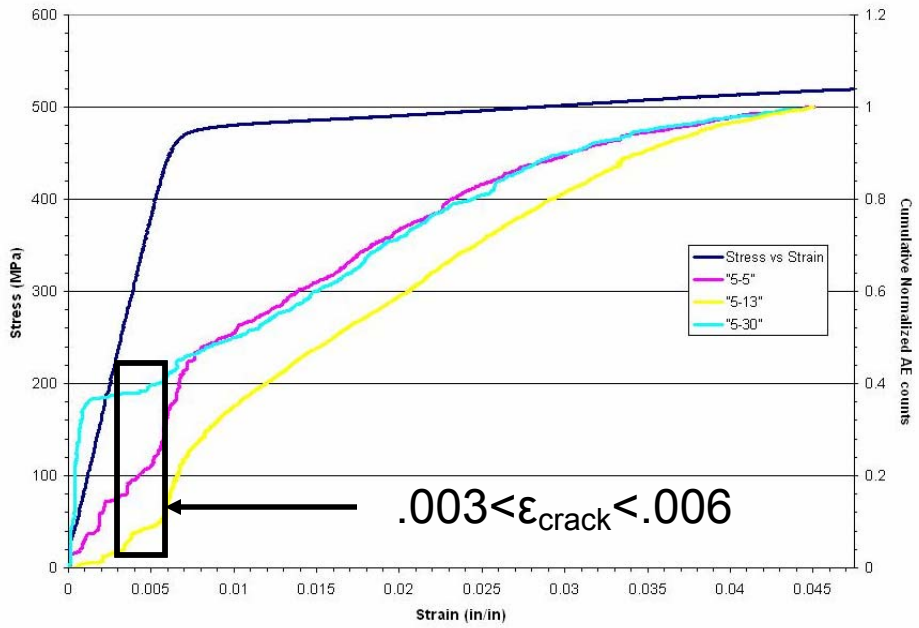

Figure 29: Cumulative normalized AE counts versus strain for all specimens with a coating thickness of 0.3-0.5 mil

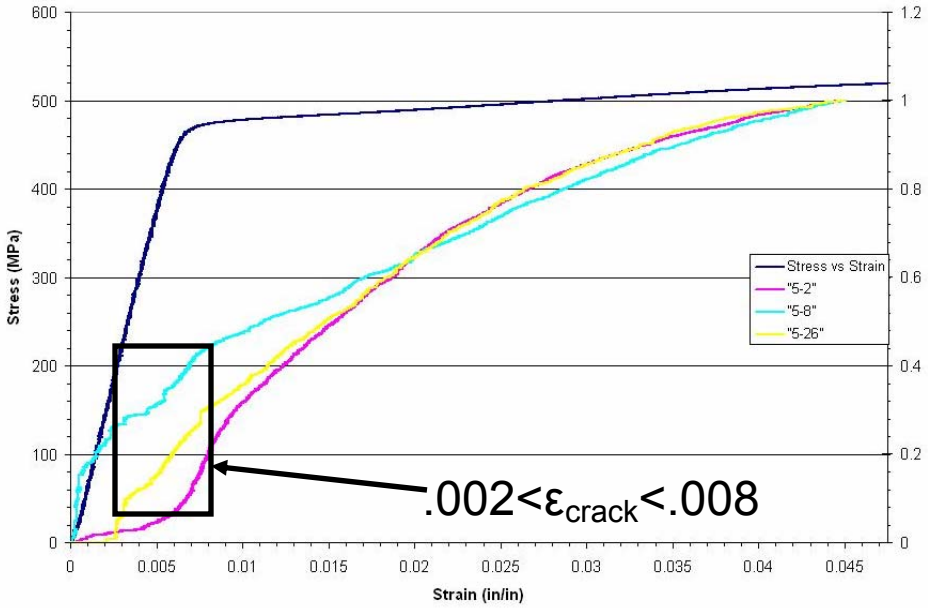

Figure 30: Cumulative normalized AE counts versus strain for all specimens with a coating thickness of 0.5-0.7 mil

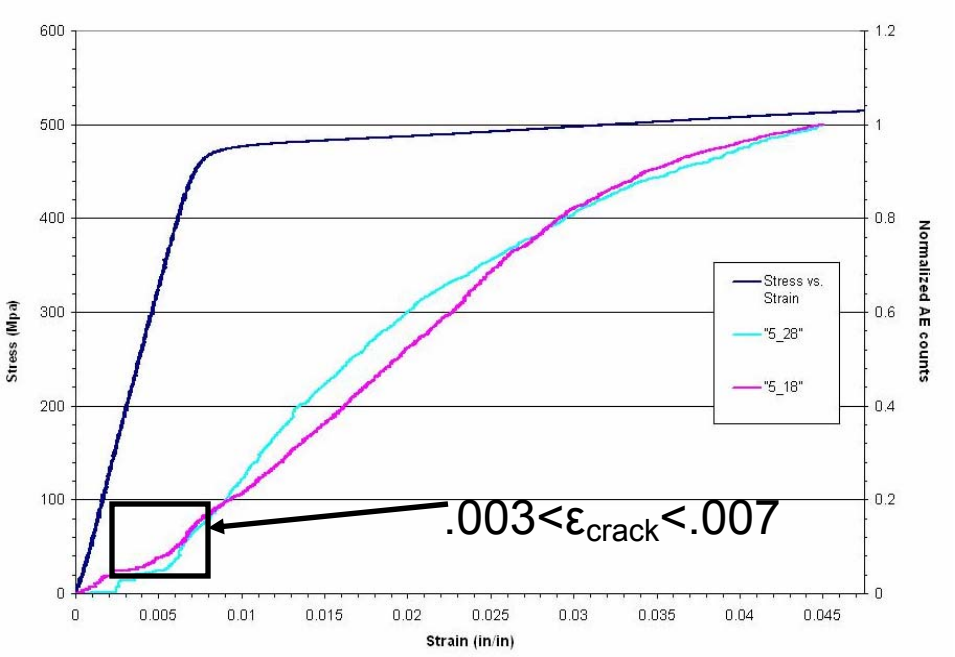

Figure 31: Cumulative normalized AE counts versus strain for all specimens with a coating thickness of 0.7-0.9 mil

For each of the plots in Figures 28-31, the stress versus strain response is typical for the deformation of aluminum. There is initially a linear elastic region followed by yielding and plastic flow. The slope of the linear portion of the stress-strain curve is given in each plot and is consistent with the modulus of 7050-T74 aluminum [17]. It should be noted that each of the experiments was halted before failure or necking of the specimen occurred.

In the plots, normalized cumulative counts are given on the right-axis. The cumulative counts were normalized by dividing each value by the total number of counts at 4.5% strain. Since the total number of counts will vary for each experiment regardless of coating thickness, the normalization procedure allowed for better comparison of the shape of the cumulative count curves. Figures 28-31 indicate that after normalization, the AE results are relatively self-similar for each coating thickness or, in other words, are generally repeatable. A comparison of a normalized cumulative count curve for each thickness is given in Figure 32. It is noted that the curve for 0.0-0.2 mil coating thickness is quite different from the curves for the other three thicknesses. This difference is related to the lower AE threshold used for the thinnest coating. However, more

fundamentally, the thinner coatings were much quieter and there might be differences in how the transverse cracks propagate.

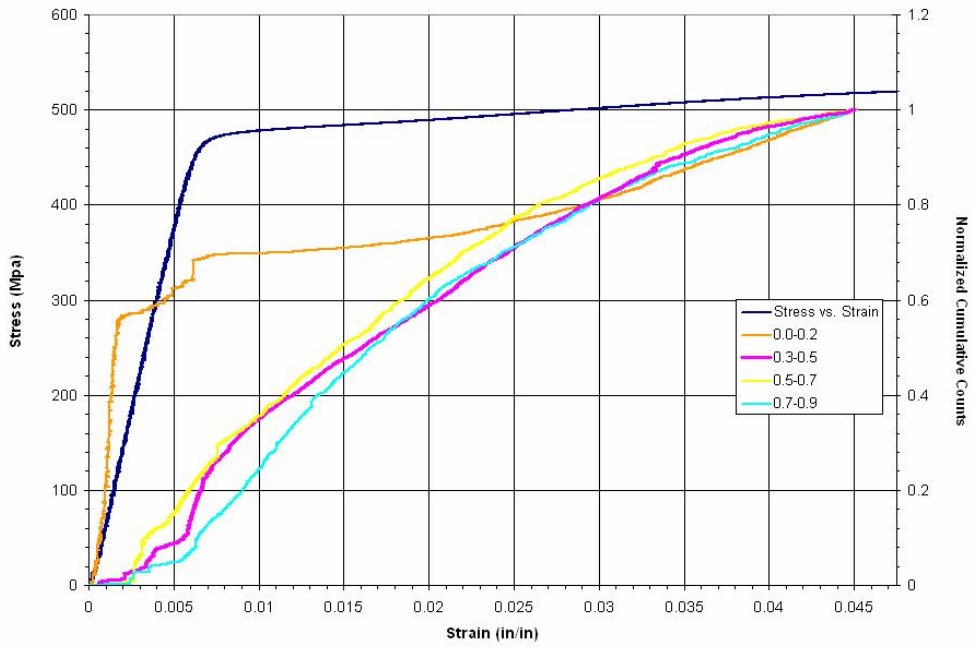

Figure 32: Normalized cumulative AE counts for four coating thicknesses

It is expected that when significant cracking is occurring there is also significant AE activity. In addition to near continuous hits, one would also expect hits with large numbers of counts. Therefore there should be vertical jumps in the normalized cumulative counts curves when cracking is occurring. Further arguments that support this hypothesis can be made by comparing the normalized cumulative count curves with the crack density plot shown in Figure 11. There are similarities between these curves and thus it might be reasonable to assume that cumulative AE results are related to crack density evolution.

From Figures 28-31, it was not possible to consistently determine the strain at which sharp vertical jumps in the cumulative AE data occurred. To overcome this, Figures 28-31 were used to determine possible regions within which cracking events are most significant. These regions are indicated in the figures, and it is also noted that there is overlap between the regions.

From looking at the raw AE data, it was possible to record the lowest strain, ε_f, for any hit that had a given number of counts. This was done for 50, 100, 150 counts and the results are shown in Figure 33.

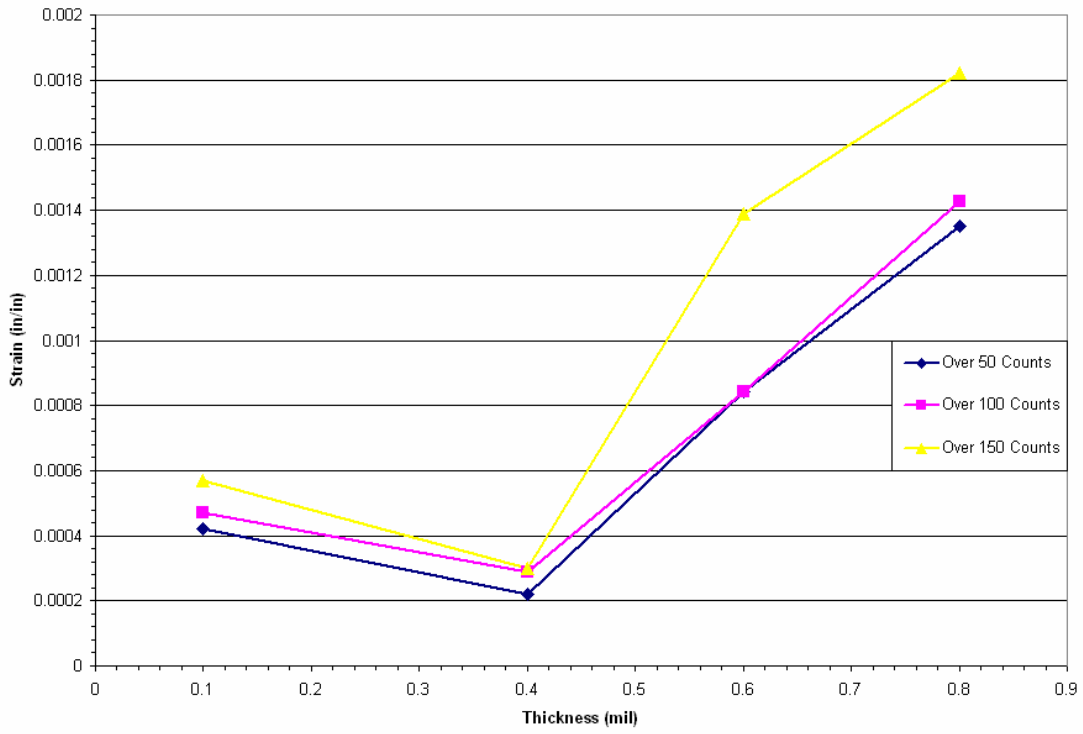

Figure 33: Strain at first AE event with high numbers of counts versus coating thickness

This plot shows that the strain at which cracking first occurs is relatively constant for the 0.0-0.2 and 0.3-0.5 mil coating thicknesses. However, the strain at which first cracking occurs increases sharply for the 0.5-0.7 and 0.7-0.9 mil coatings. These results for ε_f are also given in Table 1.

Using SEM, measurements of the maximum inter-crack spacing, λ, can be made by utilizing a simple transverse crack counting method. This method is illustrated in Figure 34. First, a 5 mil line was superimposed on the SEM images. Then the number of transverse cracks crossing each measurement line was recorded. The magnification for each photo was fixed at 500 times. In addition, for each of the four photos, five 5 mil line counts were taken to account for any variability in crack spacing. Thus a total of 20 counts per specimen were recorded and averaged. All of the counts for each coating

thickness range were then averaged and tabulated in Table 1. The ranges given in the table are for 95% confidence intervals. The average number of cracks per 5 mils was then converted to intercrack spacing (length/crack). From the data in Table 1, it is evident that the thicker coatings exhibited lower crack frequencies and therefore a higher inter-crack spacing. This point is further illustrated by comparing the number of transverse cracks in Figure 34 (0.0-0.2 mil coating thickness) and Figure 35 (0.7-0.9 mil coating thickness).

Coating Thickness, δ (mil)	ε_c	Average cracks/5 mil with 95 % confidence	Average Crack Spacing λ (mil/crack)	$\delta\varepsilon_c/\lambda$
0.1	0.00049	15.3 ± .016	0.33	0.00015
0.4	0.00027	10.5 ± 0.010	0.48	0.00023
0.6	0.0010	8.7 ± 0.013	0.58	0.0011
0.8	0.0015	7.9 ± 0.012	0.63	0.0019

Table 1: Table showing ε_c and calculation of average inter-crack spacing

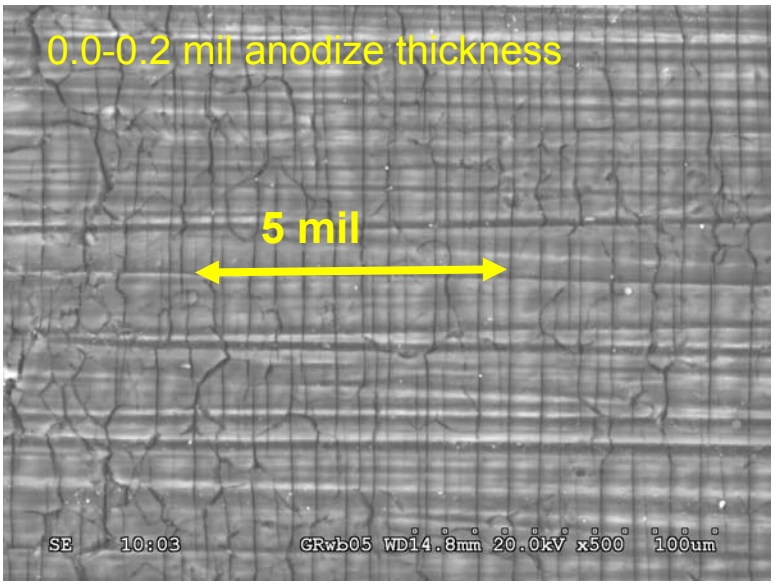

Figure 34: Transverse crack counting for 0.0-0.2 mil anodize coating

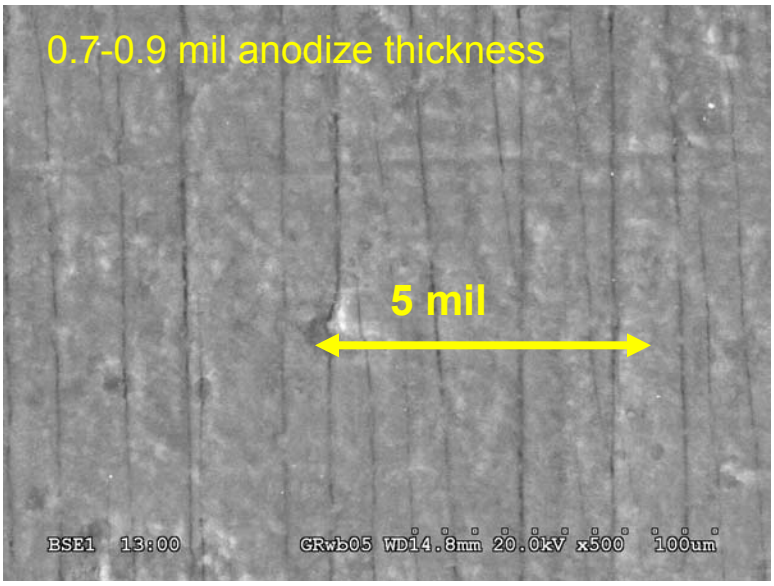

Figure 35: Transverse crack counting for 0.7-0.9 mil anodize coating

In Figure 34, it is noted that, in addition to the transverse cracks, there are also non-contiguous cracks in random orientations. These non-contiguous cracks are known as "mud cracks." Mud cracks appeared in non-uniformly stressed regions of specimens that were pulled very close to failure. In addition, as shown in Figure 36, mud cracks were present in the 0.0-0.2 mil coating specimens that were untested. Figure 37 shows the

surface of an untested 0.7-0.9 mil thick coating and it is seen that there are no mud crack patterns. Because the mud cracks in the 0.0-0.2 mil specimen (Figure 34) do not interact with the transverse cracks in the figure, it appears that they do not extend through the thickness of the anodize coating. Although a more complete examination of this phenomenon is warranted, it appears that this phenomenon is related to coating thickness and takes place during the anodizing process.

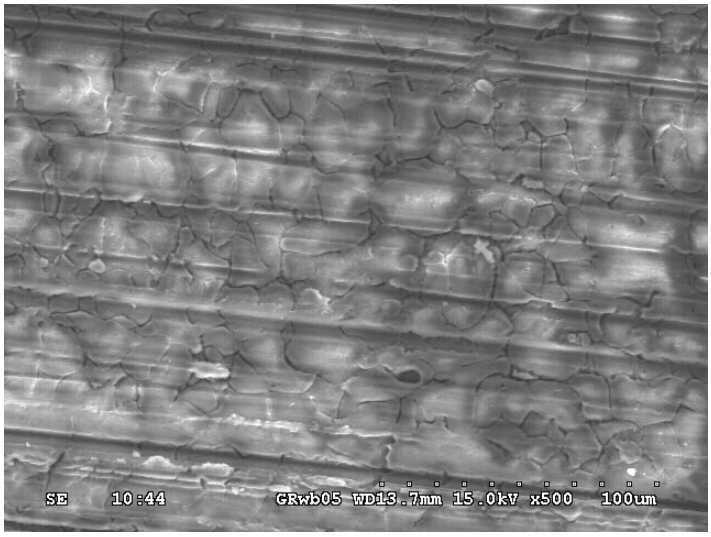

Figure 36: "Mud-Cracking in untested specimen with 0.0-0.2 mil anodize coating

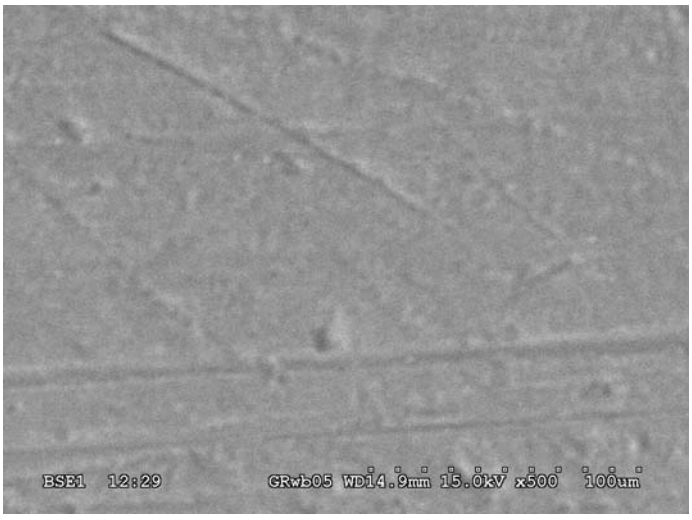

Figure 37: Untested anodize surface for 0.7-0.9 mil coating thickness

Recall from Equation 4 that ultimate interfacial shear stress of the coating is given by $\tau = \frac{E_c \varepsilon_f \delta \pi}{\lambda}$. From the results of the AE experiments ε_f has been determined. From the SEM measurements λ is known and δ is known for each specimen. If π and E_c are assumed constant, then the $\frac{\varepsilon_f \delta}{\lambda}$ term is proportional to the maximum interfacial shear strength. This term is given in Table 1 and is also plotted versus coating thickness in Figure 38. The increasing maximum interfacial shear stress with increasing coating thickness was not expected based on the crack spacing measurements. Since the spacing for the thinner coatings was substantially less, one would have expected that the thinner coatings had the higher interfacial shear stresses. However, the crack spacing effect is offset by the strain to cracking and the coating thickness, and it is the thicker coatings that have higher interfacial shear stresses. It is not known at this time how the results are affected by the assumption of constant coating modulus.

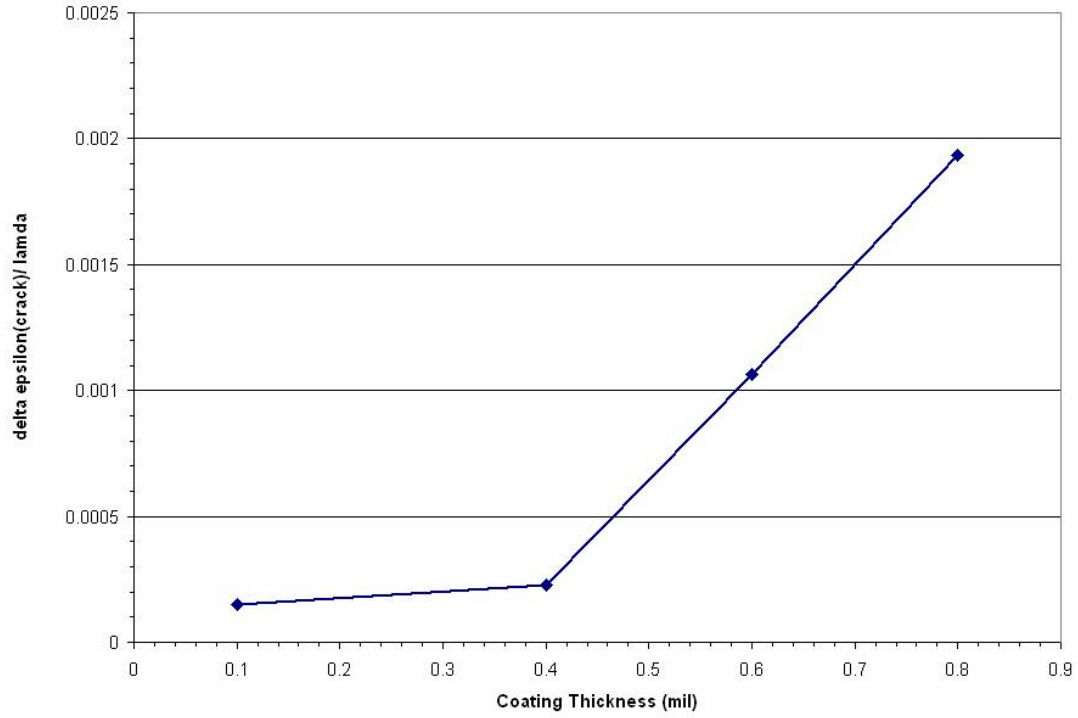

Figure 38: $\frac{\varepsilon_f \delta}{\lambda}$ versus anodize coating thickness

4.3 Correlating Fatigue and Tensile Cracking/Overall Project Results

It is noted that the fatigue experiment showed that specimens with thicker anodize coatings had reduced fatigue lives (See Section 4.1). The tensile cracking results indicate that the thickest coatings have the highest interfacial shear stresses. These results assume that the coating is ideal and without defects. It is likely that the two sets of results are related. In particular, as shown in Figure 39a, when a crack develops in the thinner coating, since the interface does not support very high shear stresses, the crack can deflect along the interface. On the other hand, as shown in Figure 39b, for stronger interfaces, cracks in the coating will more readily propagate into the base material. This relationship between fatigue strengths and tensile cracking has not been confirmed with microscopy. In addition, it is likely that there are many other factors affecting whether cracks are more likely propagate into the base material. For example, since anodizing causes part of the substrate to be sacrificed, the microstructure at the coating interface is likely to be different for different coating thicknesses. It is also likely that coatings with different thicknesses have different amounts of residual stresses. The data also has shortcomings for the two thinnest coatings. Although the two thinnest coating were determined to have similar interfacial shear stresses, the 0.3-0.5 mil coating has significantly reduced fatigue life. It is likely that the effect of coating modulus and the effect of near-interface microstructural modification will have the most significance for the thinnest coatings. In addition, the "mud cracking" discussed in the previous section may also be affecting the results of the interfacial shear stress calculation.

(a) Thin Coating (b) Thick coating

Figure 39: Schematic illustrating an explanation of the fatigue and tensile cracking results

5. Summary and Future Work

Specimens with the four anodize coating thicknesses ranges were tested in rotating cantilever beam fatigue loading. The specimens with the thinnest coatings were in the 0.0-0.2 mil thickness range and clearly had the longest fatigue lives. Specimens in the next two thickness ranges of 0.3-0.5 and 0.5-0.7 mil showed a significant reduction in fatigue life. The thickest coating with a thickness in the 0.7-0.9 mil range had a similar fatigue life as compared to the 0.5-0.7 mil coating, indicating that increasing the coating thickness beyond 0.5-0.7 mil does not have as drastic a reducing effect on the fatigue life. The failure surfaces of all coating thicknesses were characterized by with scanning electron microscopy (SEM) and surface initiation sites and defects in the coating were examined. The number of initiation sites depended on the stress amplitude of the experiment. For all specimens with single initiation sites, failure initiated from a defect in the coating. Although the results for the first three coating thicknesses ranges are very clear, increasing the sample size would increase the statistical power of the results. In addition, more samples would help to prove whether the fatigue life is really no longer reduced by anodize coating thicknesses greater than 0.5-0.7 mil.

Acoustic emission data taken during the tensile cracking experiments suggests that the strain at the onset of transverse crack formation is constant for the first two coating thickness ranges and increases for the next two coating thickness ranges. These results were based on locating hits with large counts. These large-count hits were assumed to indicate that large-scale cracking was underway. Measurements of the crack spacing of the transverse cracks, λ, were taken for each thickness range using SEM techniques. Since the coating thicknesses are known, with the assumption of constant coating modulus, it was possible to apply shear lag theory to determine values that are proportional to the maximum interfacial shear stress for each coating. These measurements indicated that the coatings in the two lowest thickness ranges had nearly constant interfacial shear stress and the next two thicker coatings showed increasing interfacial shear stress.

It may be possible to correlate the results of the tensile cracking and fatigue experiments. One possible conclusion is that as fatigue cracks form in the coating, they are more likely to propagate into substrate material if there is a strong bond between the

coating and the substrate. Otherwise, the fatigue cracks may propagate along the interface. Specimens with cracks that propagate along the interface would have longer fatigue lives. There are many variables that are not accounted for in this simple conclusion. For example, specimens in the thinnest coatings range showed "mud cracking," and it is known that anodizing for different periods of time effect the microstructure near the interface. In addition, the role of coating defects is not examined in the context of relating tensile cracking and fatigue results.

There are a number of investigations that could be undertaken to more fully understand the effects of anodize thickness on mechanical properties. In addition to detailed microscopy of coating defects, coating interfaces, and "mud cracking, residual stresses should be characterized. The residual stresses could be determined by measuring the curvature of aluminum wafers and using Stoney's Equation. To improve the tensile cracking results, it is anticipated that a semiconductor strain gage would give more accurate measurements of the strain to cracking. Not only is a semiconductor strain gage more sensitive to small strains, but it might also show jumps due to propagation of individual cracks beneath the gage. Finally, in order to truly optimize the anodize coating thickness for 7050-T74 aluminum alloy, a study of corrosion protection for each thickness level should be conducted.

References

[1] Online 04 March 2004. "Electrochemistry Encyclopedia". <http://electrochem.cwru.edu/ed/encycl/art-a02-anodizing.htm#bib>

[2] Apgar, L. and Brandeiwe, B. Presentation, "Goodrich Corporation Aircraft Wheels and Brakes Troy, Ohio" February 2004

[3] Sanford, R.J., Principles of Fracture Mechanics. Prentice Hall. Upper Saddle River, NJ. 2003.

[4] Collins, Jack A., Mechanical Design of Machine Elements and Machines: A Failure Prevention Perspective. John Wiley & Sons. Hoboken, NJ, 2003.

[5] Callister, William D. Materials Science and Engineering: An Introduction. John Wiley & Sons. New York, NY. 2003.

[6] Brown, Theodore, Bruce Bernstein, Julia Burge, and H. Eugene LeMay. Chemistry: The Central Science-Seventh Edition. Prentice Hall. 2003.

[7] Snogan, F., Blanc, C., Mankowsky, G., and Pebere, N., "Characterisation of sealed anodic films on 7050 T74 and 2214 T6 aluminum alloys," *Surface & Coatings Technology 154 ,* France, November 2001, pp. 94-103Aluminum

[8] Online 31 March 2004. Anodizers Council Web Forum. 2003. AAC. <www.anodizing.org>.

[9] Thouless, M.D., "Cracking and delamination of coatings," J. Vacuum Sci. Technology Vol. 9,No 4, New York, February 1991, pp.2510-2515

[10] Chen, B.F., J. Hwang, G.P. Yu, J.H. Huang. "In situ observation of the cracking behavior of TiN coating on 304 stainless steel subjected to tensile strain," *Thin Solid Films 35,* Taiwan May 1999, pp.173-178.

[11] Agrawal, D.C and R. Raj. "Measurement of the ultimate shear strength of a metal-ceramic interface". *Acta metal.* Vol. 37 No. 4 1989. pp.1265-1270.

[12] Yanaka, M., Y. Tsukahara, and N. Nakaso. "Cracking phenomena of brittle films in nanostructure composites analyzed by a modified shear lag model with residual strain". *Journal of Material Science 33*. Japan 1998. pp. 2111-2119.

[13] Chen, B.F., J. Hwang, I.F. Chen, G.P. Yu, and J.-H. Huang. "A tensile-film-cracking model for evaluating interfacial shear strength of elastic film on ductile substrate". *Surface & Coatings Technology 126*. Taiwan 2001. pp.91-95.

[14] Huang, Miinshiou, Liang Jiang, Peter K. Liaw, Charlie R. Brooks, Rodger Seeley, and Dwaine L. Klarstrom. "Using Acoustic Emission in Fatigue and Fracture Materials Research". *JOM 50*. November 1998.

[15] Vallen-Systeme GmbH. "Methods used against noise and interference in AE testing". Icking, Germany. 1998. pp. 1-6.

[16] Sorenson, Jim. Failure Modes, Stress Analysis, and Failure Prevention Laboratory Manual. Cop-Ez. Columbus, OH. 2004.

[17] Military Handbook - MIL-HDBK-5H: Metallic Materials and Elements for Aerospace Vehicle Structures. U.S Department of Defense. 2003.

[18] Apgar, Leslie Ph.D. Lead Materials Engineer, Goodrich Aerospace. March 2004-May 2005.

[19] Evans, Hugh and Anna Strawbridge. "Mechanical Failure of Thin Brittle Coatings". *Engineering Failure Analysis 2.* Great Britain. 1995. pp. 85-103